metals

Article

Numerical Simulation of Crack Condition in Forging Products of M50 Bearing Steel Based on Processing Map Theory

Joonhee Park [1], Byeongchan Han [1], Hyukjoon Kwon [2] and Naksoo Kim [1,*]

[1] Department of Mechanical Engineering, Sogang University, Seoul 04107, Republic of Korea; yory11@sogang.ac.kr (J.P.); hanbc1024@sogang.ac.kr (B.H.)
[2] Hanwha Aerospace Co., Ltd., 319 Pangyo-ro, Bundang-gu, Seongnam 13488, Republic of Korea; hj1985.kwon@hanwha.com
* Correspondence: nskim@sogang.ac.kr; Tel.: +82-2703-8635

Abstract: The microstructure of forged products significantly impacts their properties, and defects or carbide distribution are not visible to the naked eye. Isothermal compression tests on M50 steel with a Gleeble 3500 tester were conducted to study microstructure behavior during forging. Tests examined the hot deformation behavior within a temperature range of 900–1200 °C and a strain rate range of 0.01–10 s^{-1}. Power dissipation efficiency (η) and flow instability (ξ), which are crucial processing map parameters, were employed to analyze the high-temperature deformation behavior of M50 steel. The 3D processing map determined the optimum forging conditions, indicating that hot working should start at an initial temperature of 1050 °C or higher and a strain rate of 1 s^{-1}, decreasing the strain rate and temperature as the strain increases. The 3D power dissipation efficiency map displayed an average value of 0.43 or higher at a strain rate of 0.1 s^{-1} and a temperature of 1150 °C before reaching a strain rate of 0.8. The Finite Element Method (FEM) simulated results, revealing ξ and η distributions, and confirmed that microstructure observation during deformation matched the hot forging parameters. This approach can effectively predict microstructure changes during hot forging.

Keywords: hot forging; 3D processing map; M50 steel; intergranular crack

Citation: Park, J.; Han, B.; Kwon, H.; Kim, N. Numerical Simulation of Crack Condition in Forging Products of M50 Bearing Steel Based on Processing Map Theory. *Metals* **2023**, *13*, 921. https://doi.org/10.3390/met13050921

Academic Editor: Zbigniew Pater

Received: 16 April 2023
Revised: 28 April 2023
Accepted: 8 May 2023
Published: 9 May 2023

1. Introduction

Aerospace engines operating at high temperatures of 300–350 °C are made of bearing steels with excellent heat resistance. M50 steel has been used worldwide in manufacturing bearings, camshafts, gears and other aircraft engine parts due to excellent thermodynamic properties such as fatigue, high-temperature strength, corrosion resistance, thermal stability and hardness [1–5]. Alloying elements and carbides are related to the excellent properties of M50 [2,6,7]. However, M50 material has low hot working plasticity and is vulnerable to forging defects. Because of this performance, M50 subjected to plastic deformation can only be done in restricted hot working conditions [8]. The hot forging process of the bearing ring is a non-uniform deformation process, resulting in a non-uniform distribution of grain size. Therefore, it is essential to understand the evolution mechanism of the microstructure in the forging process. The study of the hot deformation behavior of M50 steel is necessary for optimizing the hot working process and microstructure control.

Defects due to plastic deformation are mostly caused by temperature imbalance between the material surface and the center of the material in contact with the die in the forging process [9]. The plastic behavior of the steel is determined by the high temperature, strain and strain rate [10–13]. The workability of materials deteriorates in hot deformation, not at the optimal strain rate and temperature [14]. Due to the characteristic of the forging process, errors can occur between forged products because they are often created based on the operator's experience. Since a lot of trial-and-error and cost are burdened with accumulating the operator's experience, it is necessary to design an efficient forging process to improve.

Frost and Ashby proposed the thermal deformation process theory to identify the defects caused by the strain, strain rate and temperature during processing [15]. The dynamic material model (DMM)-based instability criterion is grounded in the extremum principles of irreversible thermodynamics applied to the continuum mechanics of large plastic deformation, as described by Ziegler [16]. Kumar [17] and Prasad et al. [18] developed a modified processing map following the principles of DMM. There are flow instability criteria of Gegel [19], Murty et al. [20,21], Malas et al. [22] and Semiatin et al. [23] for predicting microstructure defects. An instability criterion based on a DMM best predicts the unstable region [24–28]. A processing map is an essential tool for evaluating the workability of various alloys. It is also a powerful method for designing and optimizing the hot deformation process. In addition, essential parameters (strain, strain rate, temperature) representing the plastic deformation ability of the hot forging process can be predicted. Under specific conditions, the microstructure evolution mechanism and flow instability region can be observed, and the optimum deformation temperature and strain rate range can be derived. Existing processing maps have limitations in not showing the effect of strain on workability. Some researchers developed a 3D processing map according to the strain of the material to solve this problem [29–31]. Recently, Park et al. developed FEM simulation data that can plot on the 3D processing map to control process parameters, avoid flow instability and include high power dissipation efficiency [32]. Jeong et al. employed a 3D processing map and utilized a learning environment founded on a Q-learning algorithm in order to optimize processing parameters, encompassing both the temperature and stroke speed of the workpiece [33]. However, microstructural defects inside the material during plastic deformation cannot be visually detected, and few studies have been conducted on predicting and observing them.

In this study, a 3D processing map was constructed based on DMM and the flow instability criterion proposed by Prasad et al. to analyze the effect of microstructure on the power dissipation efficiency (η) and flow instability (ξ). The distribution of η and ξ calculated through numerical simulation was compared with the actual microstructure by deriving equations for the parameters required for the configuration of the processing map. The reliability of this approach was verified by the optical photographs of microstructural changes inside M50 steel that may occur during plastic deformation through numerical simulation measurement.

2. Materials Experiment Procedure

The chemical composition of the M50 steel used in this study is provided in Table 1. M50 steel specimens with dimensions of $\Phi 10 \times 15$ mm were hot compressed to a true strain of 1.0 using a Gleeble 3500 tester. Compression tests were performed at temperatures of 900, 1000, 1100, 1150 and 1200 °C and strain rates of 0.01, 0.1, 1 and 10 s^{-1} to identify various deformation behaviors of the material. A tantalum plate was used to prevent adhesion between the material and the die during the high-temperature compression test and minimize friction. Before compression, specimens were heated to the target temperature at a rate of 10 °C/s and held for 3 min to eliminate the thermal gradient. For the isothermal compression test, thermocouple monitoring controlled the deformation temperature in real time. The center of the compressed M50 specimen parallel to the compression direction, it was cut and vibration polished to investigate the microstructural defects. Figure 1 shows the initial microstructure of M50 steel taken by electron backscatter diffraction (EBSD), with an average grain size of 9.85 µm. The study aimed to explore the effects of different deformation conditions on the material's behavior and the formation of microstructural defects to better understand the hot working process for M50 steel.

Table 1. Chemical composition of the M50 steel (wt%).

Composition	C	Mn	Si	P	Cr	Mo	V
(%)	0.83	0.30	0.17	0.004	4.17	4.30	1.00

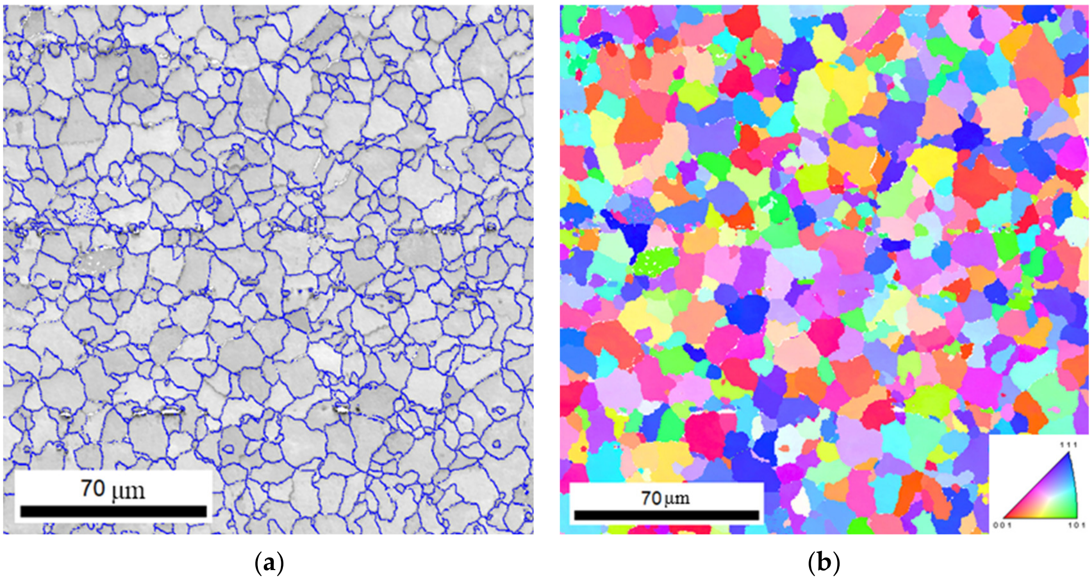

Figure 1. Initial microstructure of M50 steel captured using a SU5000 HITACHI Scanning Electron Microscope with a VELOCITY SUPER EDAX EBSD detector: (**a**) grain boundary (GB) map and (**b**) inverse pole figure (IPF) map.

To make the hot forging simulation more realistic, the temperature-dependent material properties of M50 steel are depicted in Figure 2. The measured density of M50 steel is 7810 kg/m^3. At a temperature of 876 °C, the yield strength is 128 GPa, and the Poisson's ratio is 0.26. At a temperature of 826 °C, the specific heat is 37.4 J/g·K, and the thermal conductivity is 13.6 W/m·K. Yield strength decreases with increasing temperature. As the temperature increases, Poisson's ratio decreases at 976 °C and then increases. As shown in Figure 2b, the change in the slope of Poisson's ratio in the temperature range of 900–1100 °C can be attributed to the austenitizing and phase transformation of M50 steel due to the material property changes as the temperature increases.

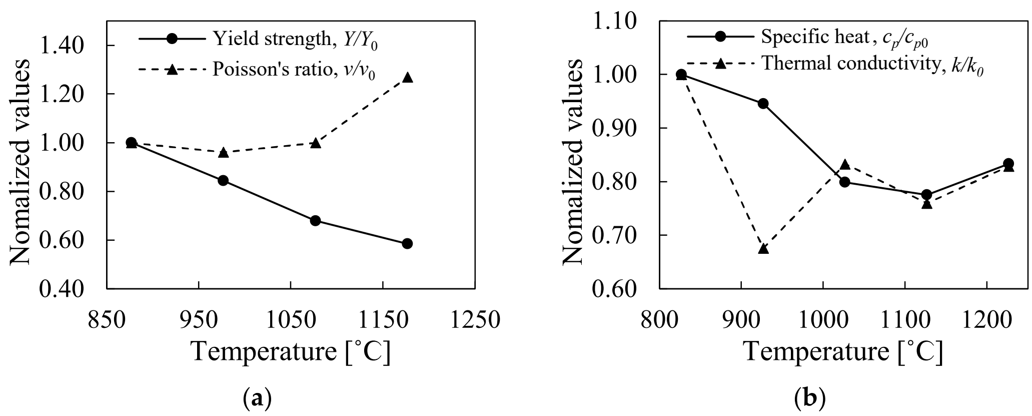

Figure 2. Temperature-dependent properties of M50 steel: (**a**) mechanical properties and (**b**) thermal properties.

3. Experiment Results

Figure 3 shows specimens compressed under various deformation conditions. The barreling phenomenon can be observed due to the friction between the surface and the die during the high-temperature compression test. During compression testing, it is impossible to eliminate the friction between the specimen surface and the die. Moreover, controlling the deformation temperature is challenging due to frictional heat and plastic deformation, which affects the target temperature. Consequently, in the flow stress curve obtained from the experiment, the flow stress may increase due to friction and decrease because of the heat generated during deformation. Therefore, modifying the experimental data to remove the effects of friction and temperature change is essential.

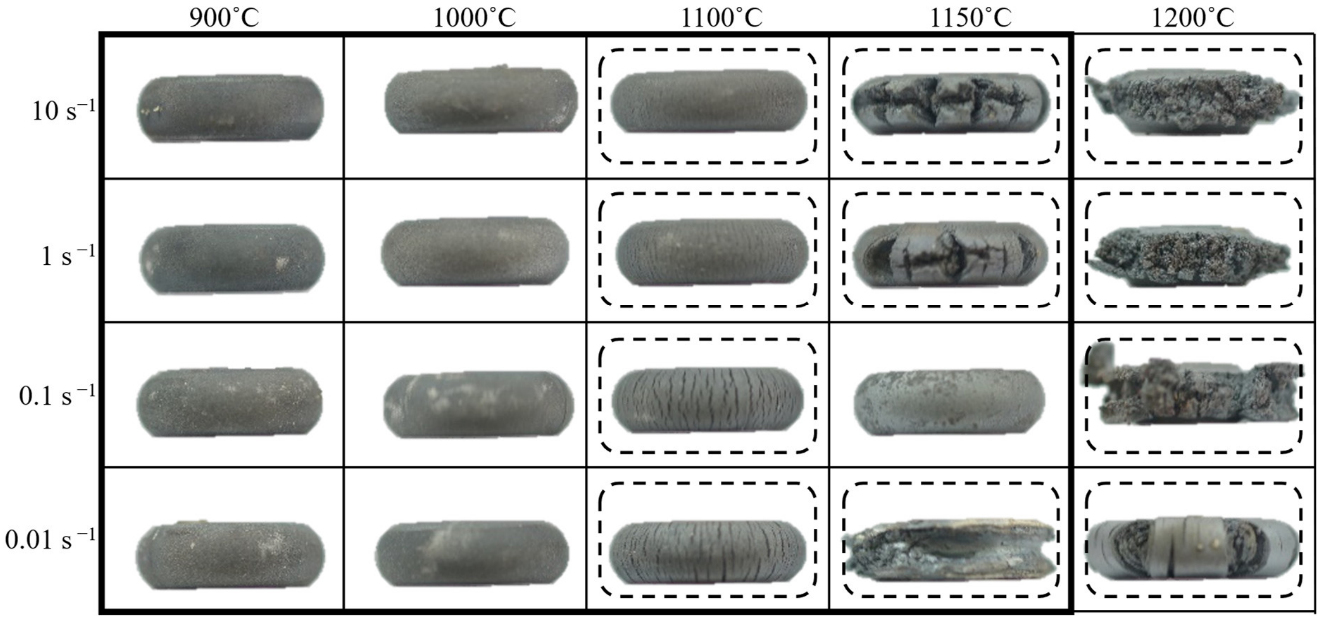

Figure 3. The surface crack condition of compressive specimens in hot deformation at strain 1.0.

The M50 steel specimen compressed to a true strain of 1.0, with black dashed lines indicating the deformation conditions in which visible cracks to the naked eye occurred externally. All the specimens compressed under the 1200 °C deformation condition showed cracks, indicating that the hot working is limited. As a result, the flow stress under the 1200 °C deformation condition was not used in constructing the processing map due to critical surface cracks. This highlights the importance of selecting appropriate deformation conditions to prevent defects and ensure the quality of the material during the hot working process.

Figure 4 shows the temperature change history measured using a thermocouple attached to the center of the specimen during the compression test. To account for the temperature-corrected flow stress, the temperature and stress relationship proposed by Park et al. [32] was linearly interpolated to match the set temperature of the isothermal compression test. To determine the friction-corrected flow stress, the correction method for determining the friction coefficient *m*, proposed by Ebrahimi et al. [34], was adopted. By applying these corrections, the experimental data can be more accurately analyzed, and the effects of friction and temperature change can be minimized.

Figure 5 shows the flow stress of M50 steel acquired from hot compression tests and the corrected curves at various temperatures and strain rates. The flow stress drop and bounce−back phenomena are observed at a true strain of 0.1 under the deformation conditions of a strain rate of 10 s^{-1} [35,36]. It is well-known that for most steels and alloys, the flow stress decreases with increasing deformation temperature or decreasing strain rate [37–39]. It was observed that the flow stress of M50 steel increases as the strain rate increases at a specific temperature. Because a high temperature rises, the kinetic energy of atoms and a low strain rate provide sufficient time for nucleation and growth of dynamic recrystallization grains. The flow stress of low strain increases rapidly with a work hardening step due to dislocation accumulation and dislocation density increasing, reaching peak stress. As strain increases, dynamic recrystallization is the main softening mechanism, and flow stress decreases. When a dynamic equilibrium between work hardening and softening is obtained, the flow stress remains constant with increasing strain. The corrected values generally appeared lower than the experimental values. The peak flow stress is over 350 MPa under the deformation condition of 10 s^{-1} at 900 °C. At a deformation temperature of 1200 °C of strain 0.6 or less, the flow stress is less than 100 MPa. Figure 5d shows that the dynamic softening of the flow stress under the deformation conditions of 1150 °C and 0.1 s^{-1} is evident.

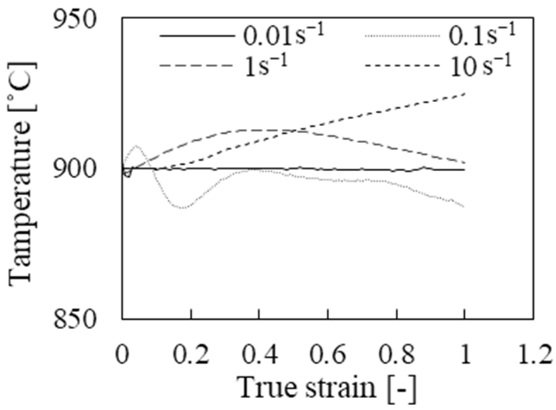

(**a**)

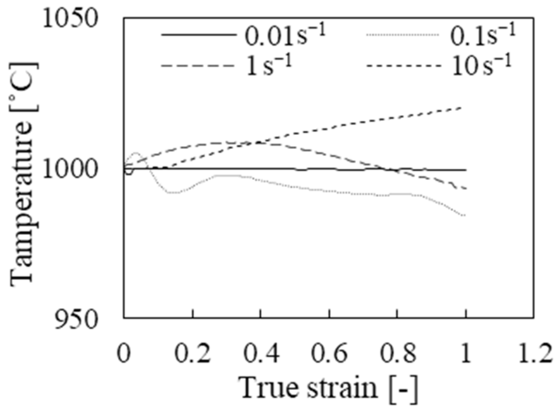

(**b**)

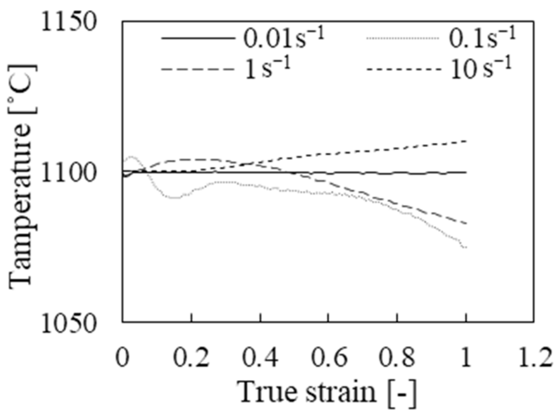

(**c**)

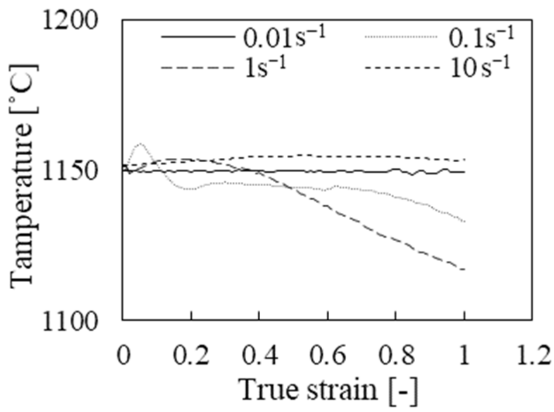

(**d**)

Figure 4. Temperature changes during the compression test based on the temperature measured by the thermocouple attached to the center of the specimen: (**a**) 900 °C, (**b**) 1000 °C, (**c**) 1100 °C and (**d**) 1150 °C.

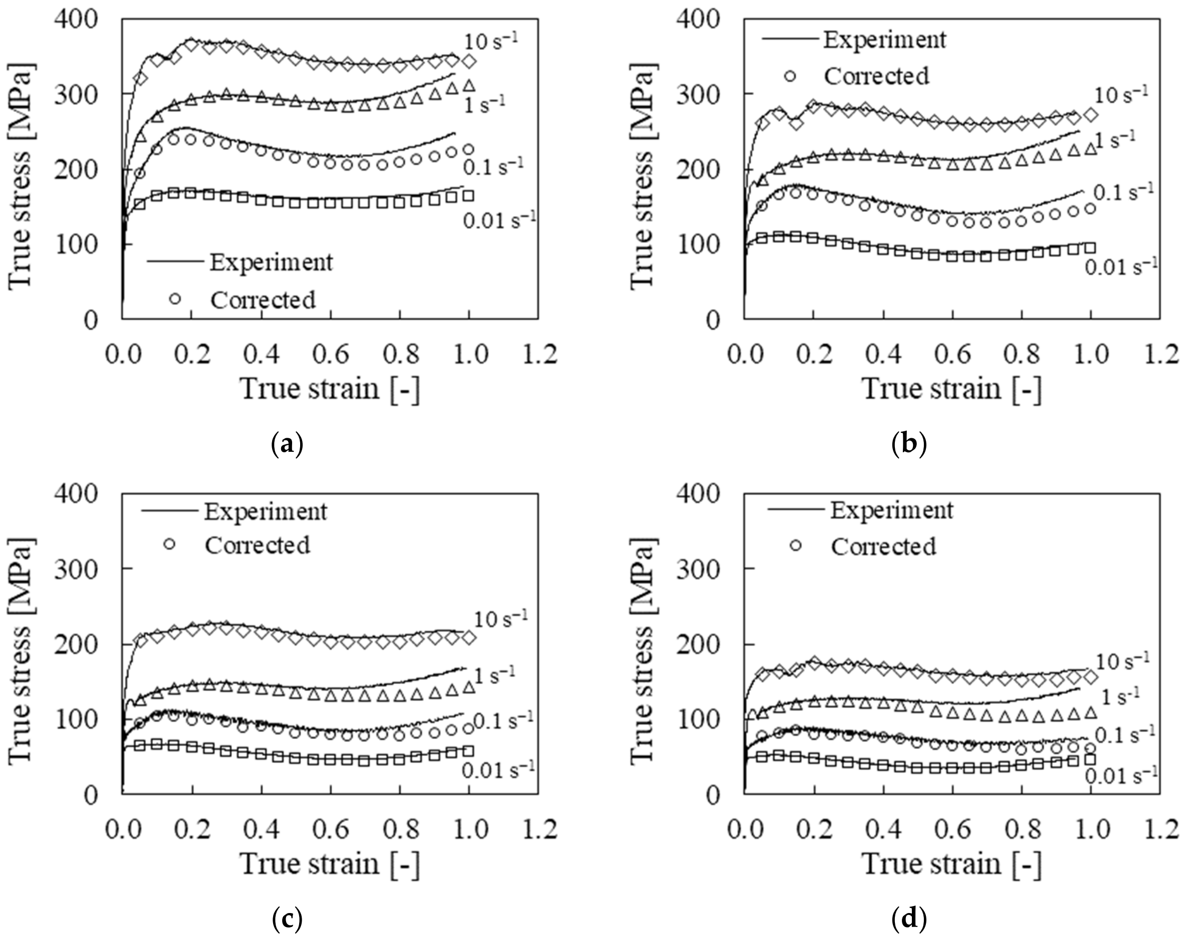

Figure 5. The true strain–true stress curve of M50 steel obtained from the compression tests deformed up to a true strain 1.0 in the strain rate range between 0.01 s^{-1} and 10 s^{-1}: (**a**) 900 °C, (**b**) 1000 °C, (**c**) 1100 °C and (**d**) 1150 °C.

4. Processing Map

4.1. Processing Map Theory

The 2D processing map according to the strain proposed by Prasad et al. consists of overlapped power dissipation efficiency and flow instability at different temperatures and strain rates [18,40]. The flow stress in high-temperature deformation of steels can be described as:

$$\sigma = K\dot{\varepsilon}^{m} \tag{1}$$

The DMM is assumed to be a power dissipator that dissipates the applied power at a constant temperature during deformation. At a specific strain rate, the total power (*P*) consists of *G* content and *J* co-content. *G* content includes power dissipated by temperature rise and plastic deformation. *J* co-content is the power dissipated by microstructural evolution such as phase transformation, dynamic recovery, and dynamic recrystallization. Therefore, the total power is expressed as follows:

$$P = \sigma\dot{\varepsilon} = \int_0^{\dot{\varepsilon}} \sigma d\dot{\varepsilon} + \int_0^{\sigma} \dot{\varepsilon} d\sigma = G + J \tag{2}$$

The *G* content and *J* co-content ratio during hot deformation are defined as strain rate sensitivity (*m*). The value of m depends on the strain and temperature for a stable material flow range, varying from 0 to 1. Equations (1) and (3) can be combined to express the total energy (P).

$$m = \frac{\partial J}{\partial G} = \frac{\dot{\varepsilon} d\sigma}{\sigma d\dot{\varepsilon}} = \frac{\dot{\varepsilon}\sigma d \ln \sigma}{\sigma \dot{\varepsilon} d \ln \dot{\varepsilon}} = \frac{\partial \ln \sigma}{\partial \ln \dot{\varepsilon}} \quad (3)$$

The power dissipation efficiency (η) is the ratio of the efficiency of a material dissipated to the maximum power dissipation through microstructure changes during the deformation process, as defined in Equation (4) [41]. It represents η via contour lines in the processing map. For the ideal plastic flow state, when m = 1, $J = G = P/2$, and J reaches its maximum value.

$$\eta = \frac{J}{J_{\max}} = \frac{\int_0^{\dot{\varepsilon}} \sigma d\dot{\varepsilon}}{\sigma\dot{\varepsilon}/2} = \frac{2m}{m+1} \quad (4)$$

The occurrence of some internal defects, such as cracks and void formation, can also have the same η [42]. To predict microstructural defects based on DMM and the extremum principles of irreversible thermodynamics as applied to large plastic flow, Ziegler [16], Kumar [17] and Prasad et al. [43] proposed a flow instability criterion (ξ).

$$\xi(\dot{\varepsilon})_{\text{Kumar}-\text{Prasad}} = \frac{\partial \ln(m/m+1)}{\partial \ln \dot{\varepsilon}} + m < 0 \quad (5)$$

The flow instability criterion determines the plastic deformation unstable condition for a given temperature and strain rate. It was developed based on the flow instability criterion derived from the limit principle of irreversible thermodynamics, and the concept of continuum criterion of large plastic flow is applied [24,44]. If ξ satisfies the inequality, unstable flow occurs [9,25,45]. The processing map is stable when flow instability zones are avoided for the best hot workability with high power dissipation efficiency. Microstructure defects of hot forming that may occur in the flow instability region are adiabatic wedge cracks, shear bands, flow localization, dynamic strain ageing (DSA), kink bands and intergranular crack [25,46–48].

The changes in η and ξ at a strain rate of 0.1 s^{-1} under various temperatures are shown in Figure 6. At a strain rate of 0.1 s^{-1}, η tends to increase as the temperature decreases and the strain increases. At a strain rate of 0.1 s^{-1}, ξ initially has a negative value in all deformation conditions except at 1150 °C and increases as the strain increases. This implies that the unstable region is avoided as the strain increases, and the possibility of microstructural defects is reduced. Generally, the higher the power dissipation efficiency of a material, the better the workability [49]. Among the deformation conditions at a strain rate of 0.1 s^{-1}, the η value is the highest at 1150 °C, and the instability (ξ = −0.0093) appears at a strain of 0.15. However, some defects may be found even at deformation conditions with high dissipation efficiency, so it is necessary to analyze both η and ξ comprehensively.

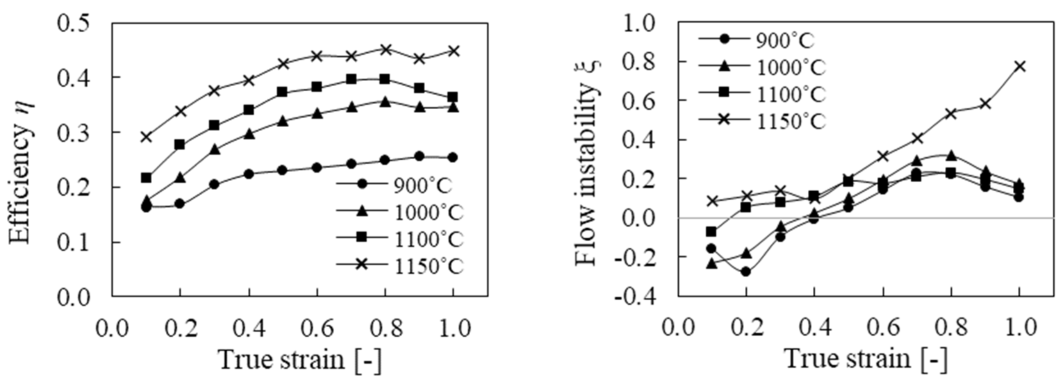

(**a**) (**b**)

Figure 6. The M50 steel at different strain rates of 0.01 s^{-1}: (**a**) efficiency and (**b**) flow instability.

4.2. Expansion of Processing Map to Include Accumulated Strain

The 3D processing map is shown in Figure 7. Stacking 2D processing maps from strain 0.1 to 1.0, according to Park et al. [32], the 3D processing map was plotted separately without overlapping η and ξ to increase visibility. According to the color depth, Figure 7a is a 3D power dissipation efficiency map stacked at 0.01 from strain 0.1 to 1.0. Figure 7b is a 3D flow instability map, and the gray area represents the flow instability zones; workability can be determined by stacking the strain from 0.1 to 1.0 at 0.05 intervals. Red circles indicate the processing conditions of the compressed specimen with surface cracks on the flow instability map. The 3D processing map was utilized to determine the parameters (strain, strain rate, temperature) in the hot forging process of M50 steel. The calculated η and ξ values in Figure 6 agree with the 3D processing map.

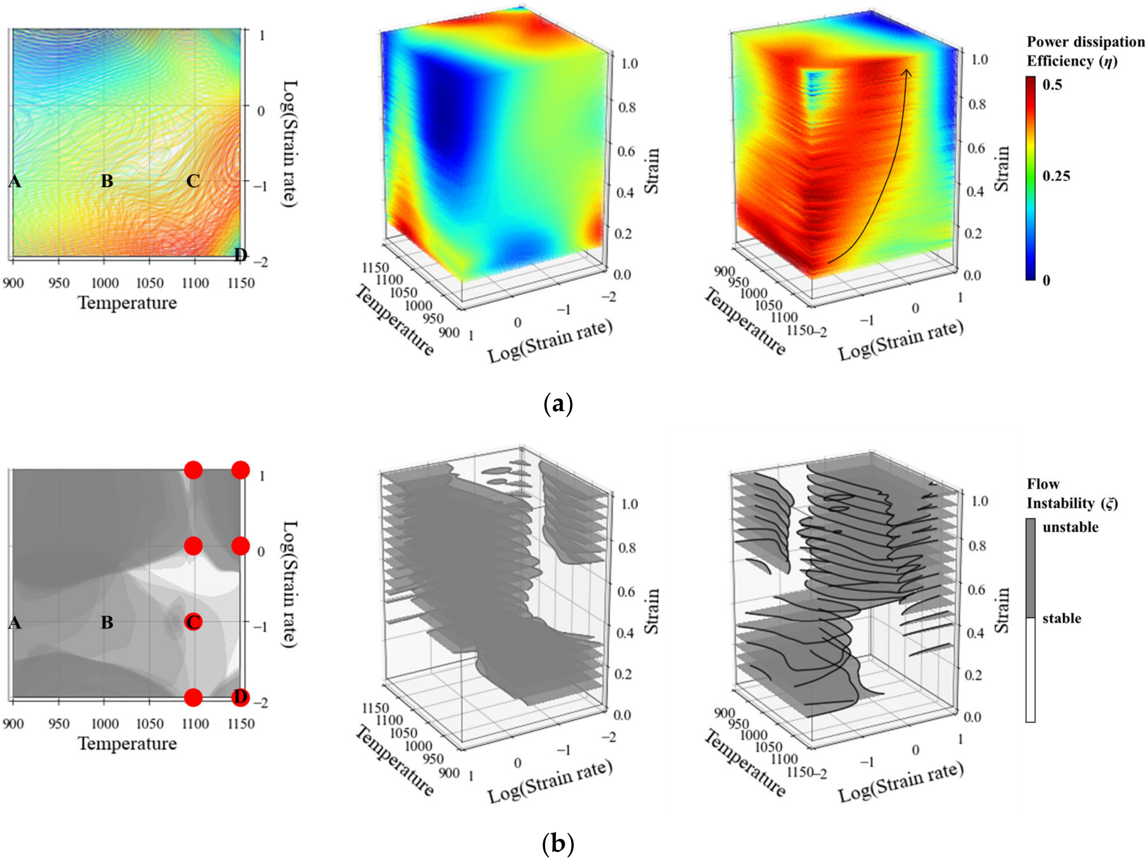

Figure 7. The 3D processing map from different angles: (**a**) power dissipation efficiency map and (**b**) flow instability map.

The power dissipation efficiency map shows an η value of 0.4 or higher as the strain and strain rate increase at temperatures of 1100 °C or above. A peak η value of 0.5 is observed at a strain of 0.4, a temperature of 1150 °C and a strain rate of 0.01 s^{-1}. This occurs due to increased DRX nucleation and particle growth, which consumes more deformation energy. At lower temperatures of 900 °C and a strain rate of 10 s^{-1}, the power dissipation efficiency exhibits a low value approaching zero. The 3D power dissipation efficiency map reveals an average value of 0.43 or higher at a strain rate of 0.1 s^{-1} and a temperature of approximately 1150 °C, up to a strain of 0.8.

As shown in Figure 7b, the gray-colored area on the 3D flow instability map indicates instability. All unpainted areas suggest stable working conditions. The unpainted area between temperatures of 1000 and 1150 °C and strain rates of 0.1 and 1 s^{-1} represents a stable working condition. Upon comparing the compressed specimens in Figure 3, it becomes evident that the external cracks generated at 1100 °C and 1150 °C occurred at strains more than 0.7. As the strain increases, the flow instability zones shift to higher strain rate regions. Therefore, the hot working condition should be induced to a process in which the temperature and strain rate decrease as the strain increases, starting from an initial temperature of 1050 °C or higher and a deformation condition of strain rate 1 s^{-1}.

This consistency demonstrates that the processing map effectively represents the hot forging process of M50 steel, capturing the relationship between strain, strain rate, temperature, power dissipation efficiency and flow instability. In Figure 8, EBSD imaging of the cross-sections of the compressed specimens for specific deformation conditions A, B, C and D, selected in Figure 8b, demonstrates that the crystal grain size increases with increasing temperature. In condition A, η increases from 0.16 to 0.26 as the strain increases, and ξ overlaps the region of strain 0.1–0.4. In condition B, η remains within the range of 0.3 to 0.34, and ξ overlaps the region of strain 0.1–0.3. For condition C, η increases from 0.36 to 0.4 as the strain increases, and ξ overlaps within a tiny strain range of 0.1–0.15. In condition D, η maintains a value of 0.4 or higher until the strain reaches 0.8 and then decreases to less than 0.3 at strains of 0.8 or higher. ξ overlaps in the strain range of 0.75^{-1}. As shown in Figure 8d, intergranular cracks are generated under these conditions. These observations highlight the importance of carefully selecting the appropriate hot forging parameters to optimize the microstructure and reduce the likelihood of defects in the final product. By using the 3D processing map and EBSD imaging, it is possible to better understand the relationship between the deformation conditions, power dissipation efficiency, flow instability and the resulting microstructure of M50 steel.

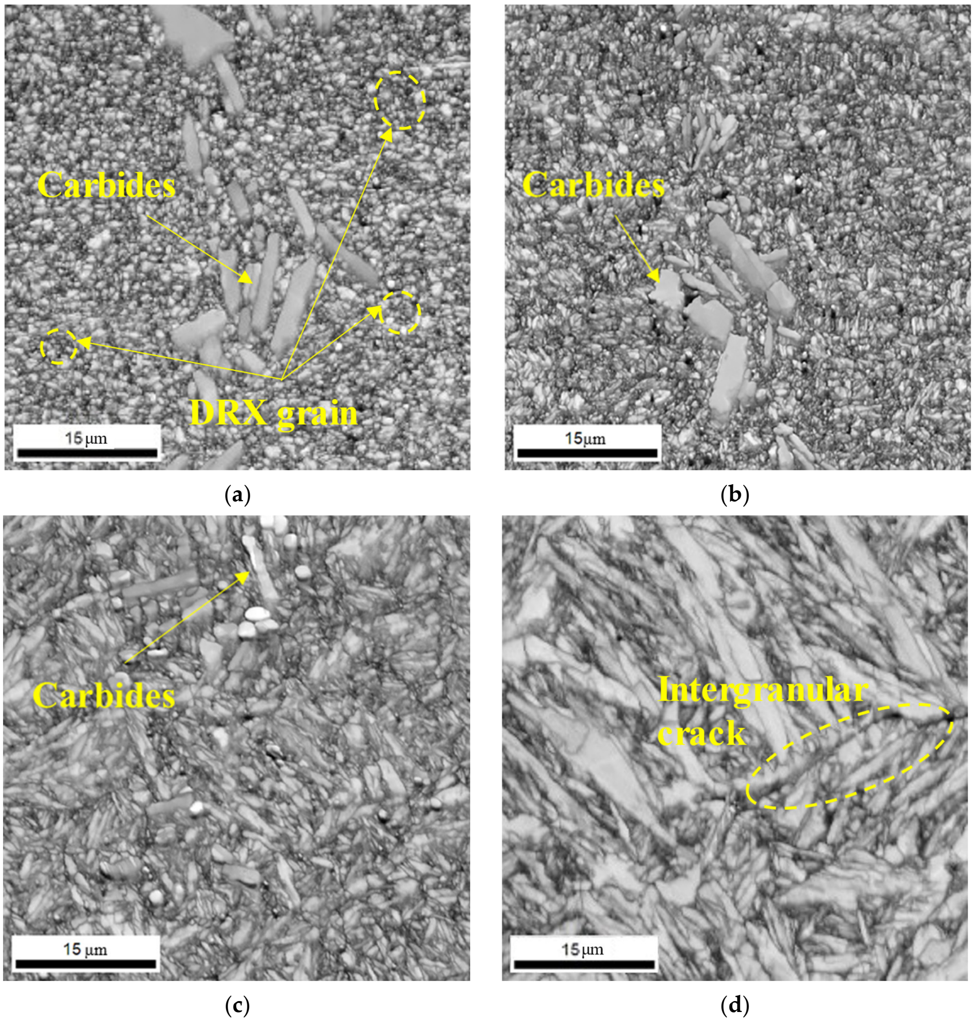

Figure 8. Microstructures of M50 steel at the strain 1.0: (**a**) 900 °C/0.1 s^{-1}, (**b**) 1000 °C/0.1 s^{-1}, (**c**) 1100 °C/0.1 s^{-1} and (**d**) 1150 °C/0.01 s^{-1}.

4.3. Numerical Simulation Based on a Processing Map Theory

The crack simulation using the commercial finite element analysis (FEA) software ABAQUS showed a crack phenomenon by applying element deletion method in conjunction with a non-local fracture criterion [50,51]. In this study, the isothermal forging process can display the distribution of η and ξ generated during deformation at various process temperatures and strain rates. The results calculated through FEM simulation and the microstructure of the high-temperature compressed specimens measured were compared to observe if there were any defects within the specimen. In FEM simulation, strain rate sensitivity (m) can be derived as illustrated in Equation (6), according to the time increment of stress and strain rate that changes in response to deformation. m is calculated using Von Mises stress and strain rate at the integration point, and power dissipation efficiency (η) of the Equation (4) and flow instability (ξ) of the Equation (5) are computed by m, mapping η and ξ to each integration point.

$$\frac{\partial J}{\partial G} = \frac{\dot{\varepsilon} d\sigma}{\sigma d\dot{\varepsilon}} = \frac{\dot{\varepsilon}\sigma d \ln \sigma}{\sigma \dot{\varepsilon} d \ln \dot{\varepsilon}} \approx \left[\frac{\Delta \log \sigma}{\Delta \log \dot{\varepsilon}}\right]_{\varepsilon,T} \equiv m \quad (6)$$

The hot forging simulation of a cylindrical sample with dimensions of Φ 10 × 15 mm was conducted using the FEA software ABAQUS 2020, as depicted in Figure 9. The material properties input for the simulation included the flow stress and mechanical and thermal properties presented in Section 2. The Coulomb friction coefficient used in the simulations was set to 0.4. The material is influenced by friction, heat exchange and other factors in the actual process, resulting in non-uniform temperature and strain within the material. Therefore, the deformable material area was divided into three regions: ⓐ, ⓑ and ⓒ. Region ⓐ is more affected by friction during the deformation process due to contact between the upper and lower dies and the material rather than by heat exchange. Region ⓑ undergoes large deformation owing to a compressive stress state and low deformation resistance. Region ⓒ, a free surface, is not influenced by friction but is affected by heat exchange.

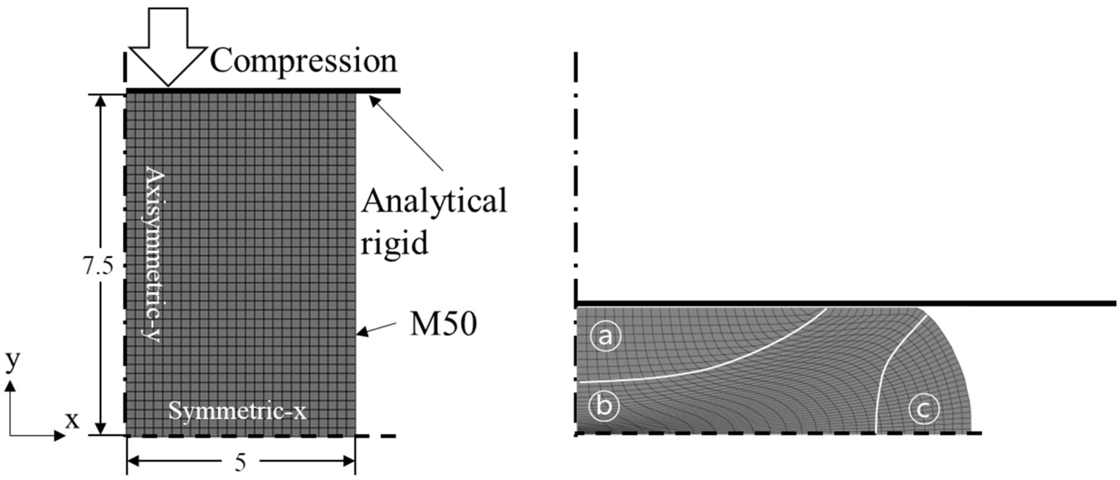

Figure 9. Schematic of cylinder forging simulation.

According to the combination of Equations (4) and (6), η can be calculated. Figure 10 displays the power dissipation efficiency distribution based on the strain under the deformation conditions of 900 °C and 0.1 s^{-1}. As the deformation during compression increases, η transitions from region ⓐ to region ⓑ, and its value rises. Region ⓐ maintains a relatively constant value as the strain increases, while η increases with the strain in regions ⓑ and ⓒ. The highest value appears in the ⓑ region at a true strain of 1.0.

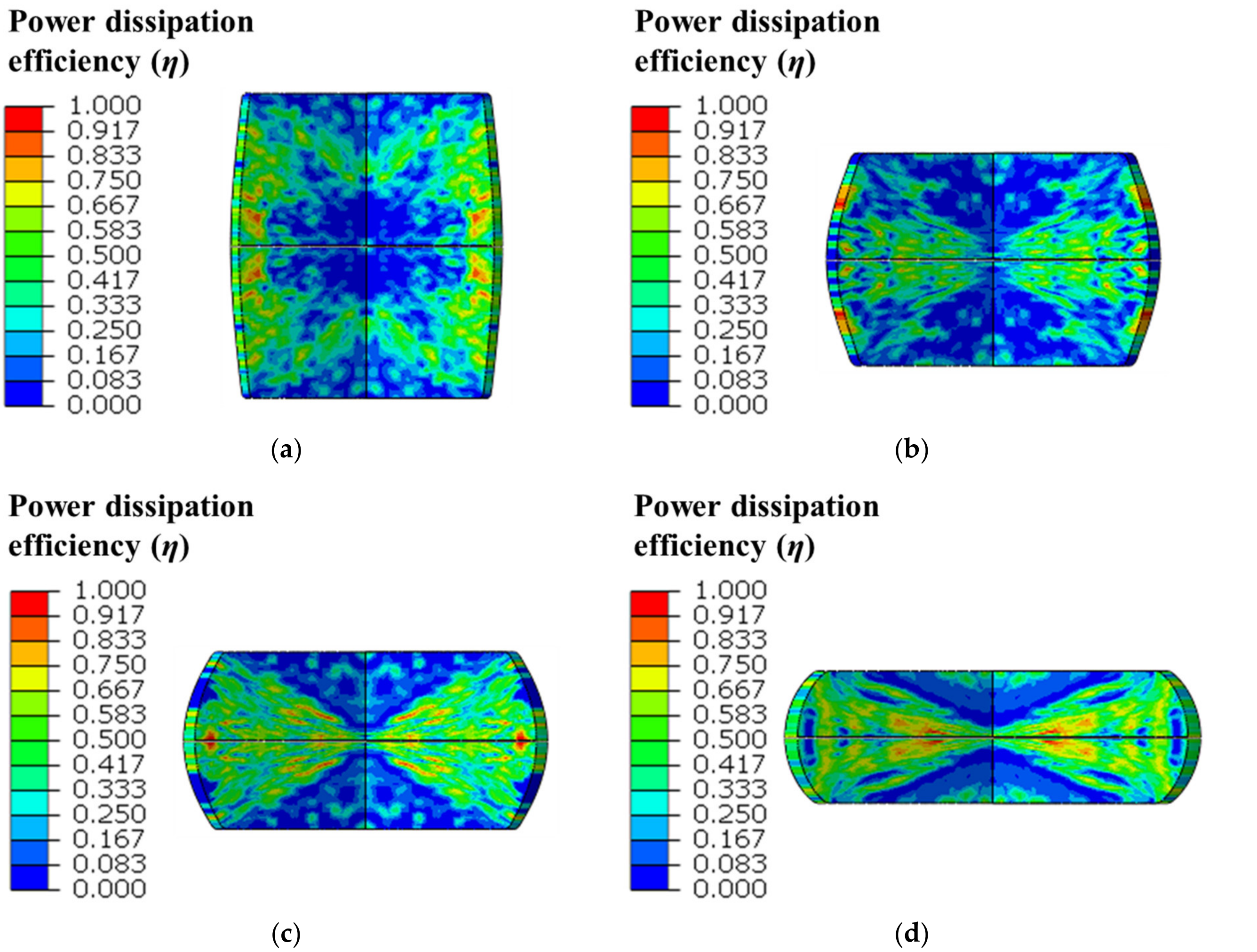

Figure 10. The distribution of power dissipation efficiency in the temperature of 900 °C and strain rate of 0.1 s^{-1} at different strains: (**a**) 0.25, (**b**) 0.65, (**c**) 0.95 and (**d**) 1.0.

By integrating Equations (5) and (6), ξ can be calculated. The results of the hot forging simulation at 1150 °C/10 s^{-1} and areas A, B, C and D selected in Figure 7b were compared with the microstructure captured using an optical microscope, as shown in Figure 12. The mesh deformation ξ and η values, based on the simulation results, are presented. The distribution of $\xi < 0$ indicates the non-flow instability area. A red dashed line signifies the location identified as a wedge crack type of microstructural defect in the microstructure photograph. On the left side of the simulation results, a similar carbide distribution flow line pattern can be observed through the shape of the deformed mesh.

The power dissipation efficiency (η) distribution for each strain rate at 1000 °C is presented in Figure 11. As the strain rate increases from 0.1 to 10 s^{-1}, the distribution of η values tends to decrease rapidly. It is because dynamic recrystallization takes longer at low strain rates. However, at high deformation temperatures, the power dissipation efficiency value decreases due to grain growth. The results are well-matched with the analysis of the 3D processing map. For each strain rate, η in the region ⓐ remains more constant than in other zones.

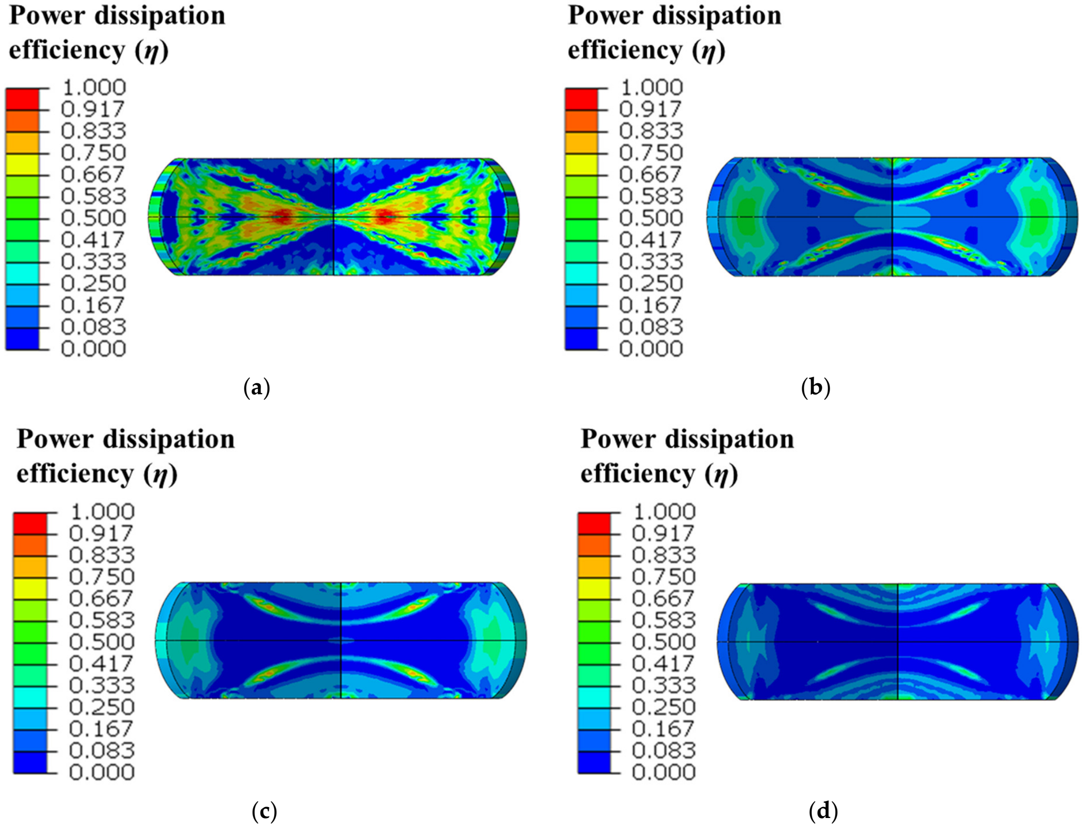

Figure 11. The distribution of power dissipation efficiency in the temperature of 1000 °C at different strain rates: (**a**) 0.01 s^{-1}, (**b**) 0.1 s^{-1}, (**c**) 1 s^{-1} and (**d**) 10 s^{-1}.

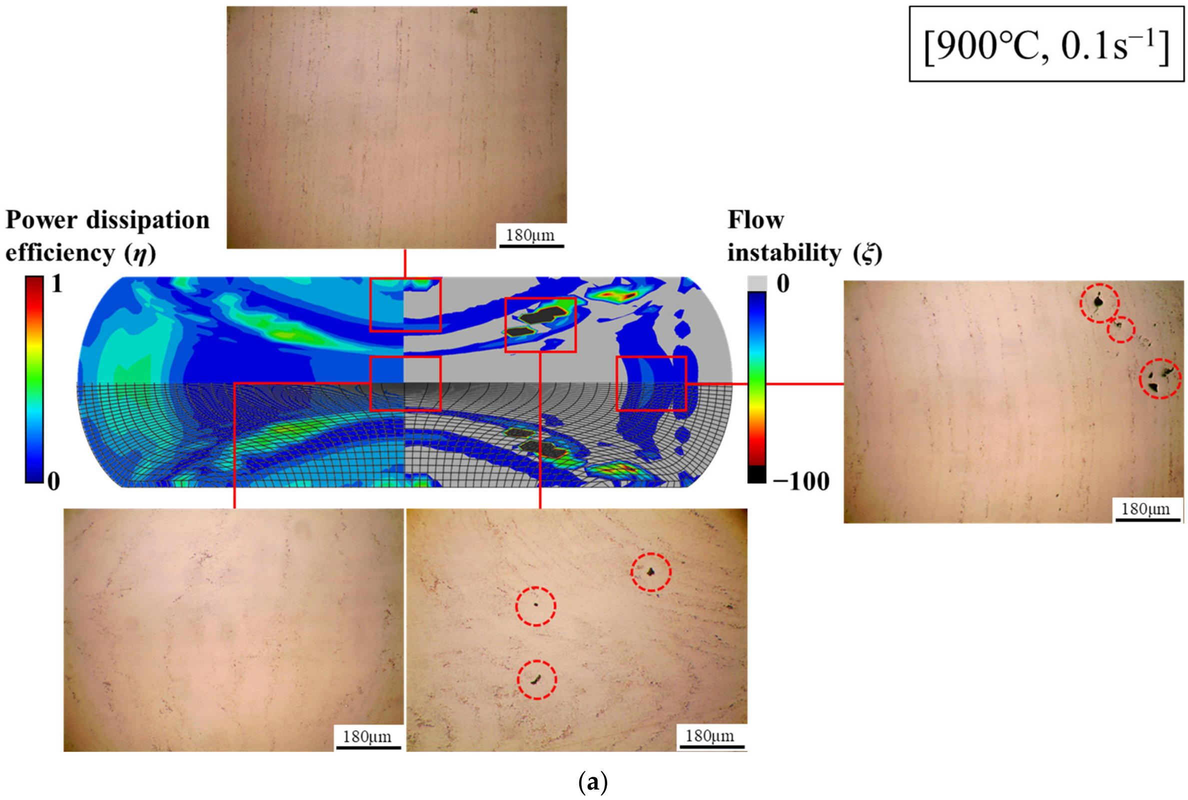

Figure 12. *Cont.*

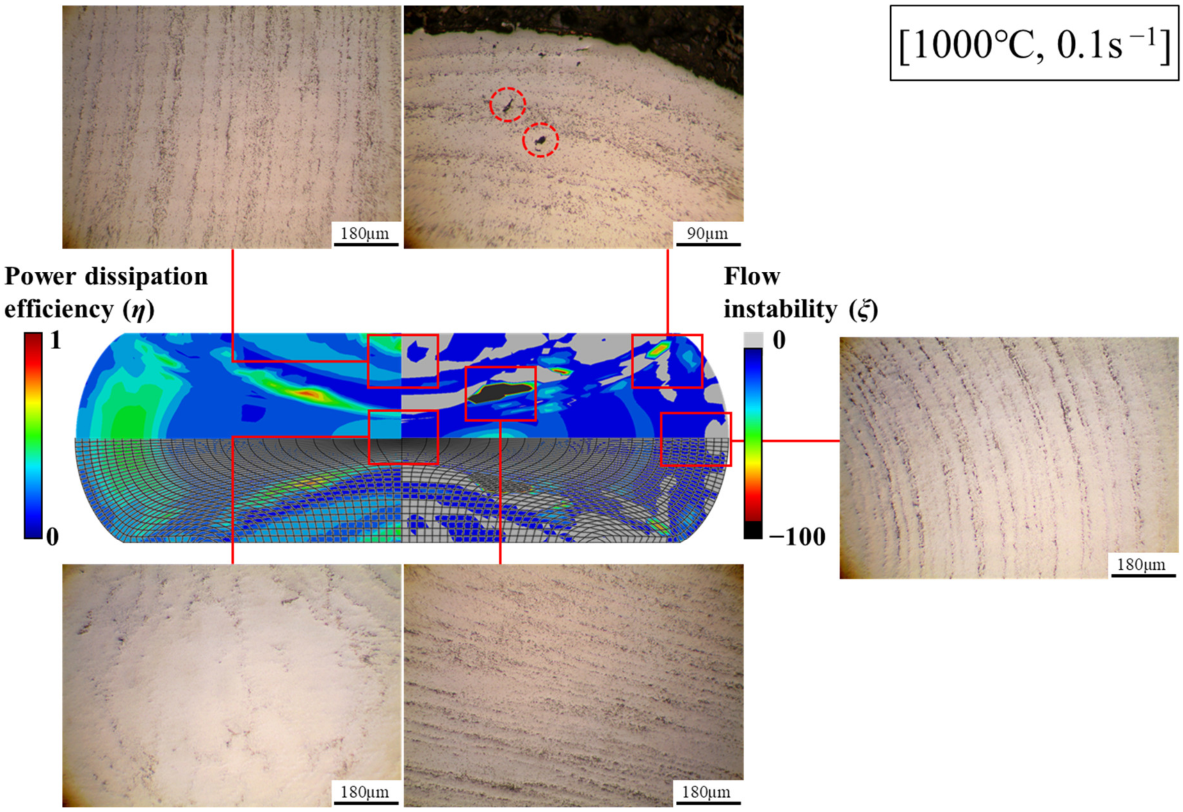

(**b**)

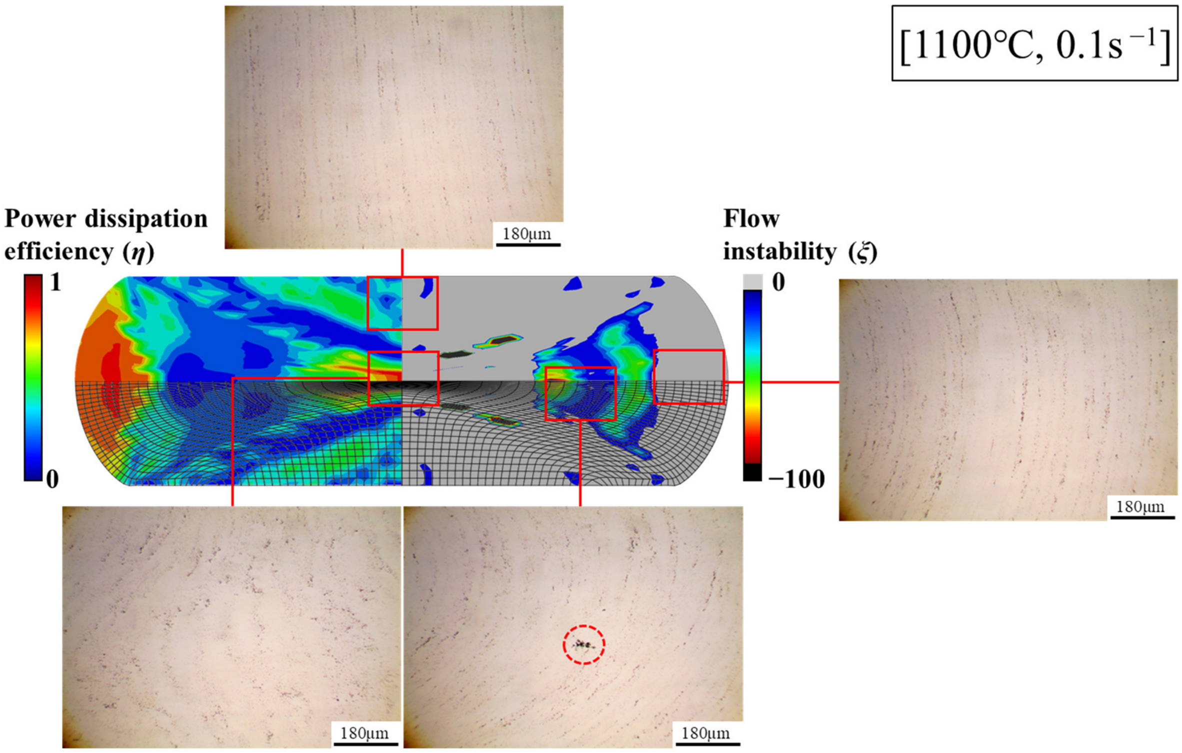

(**c**)

Figure 12. *Cont*.

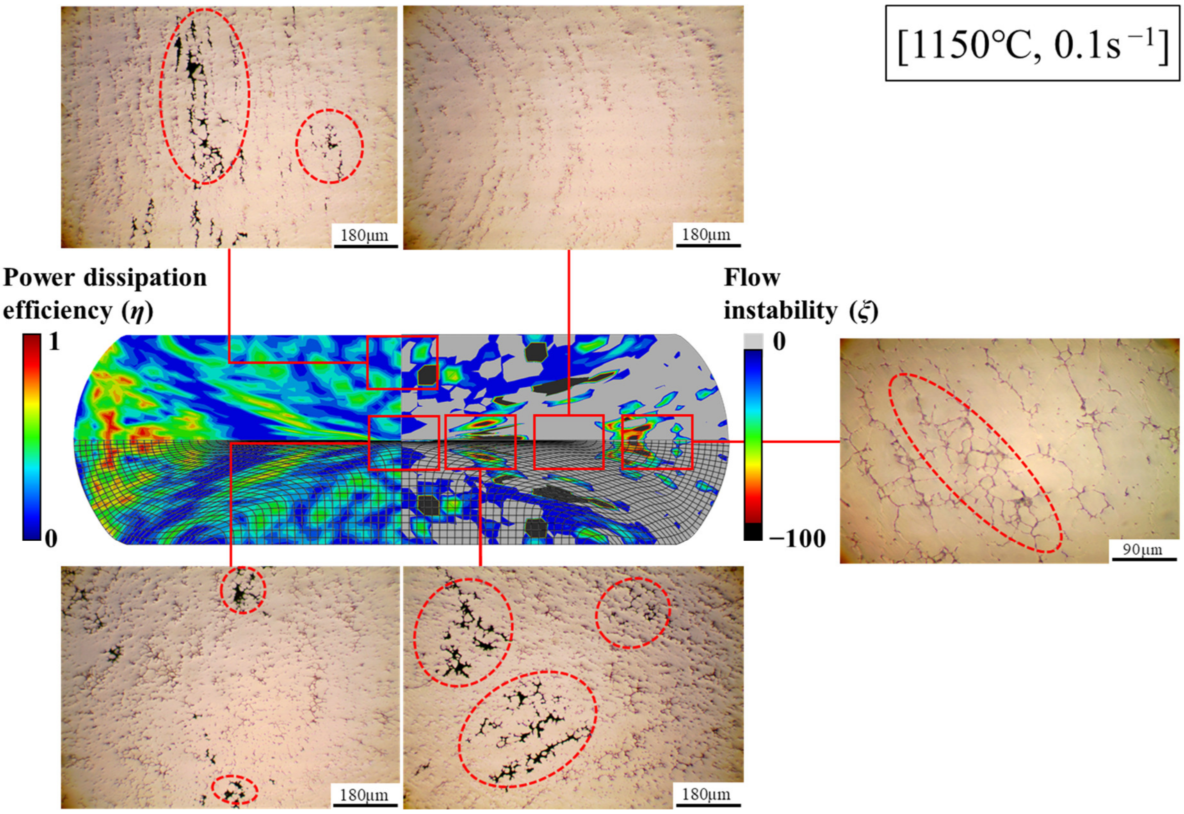

(**d**)

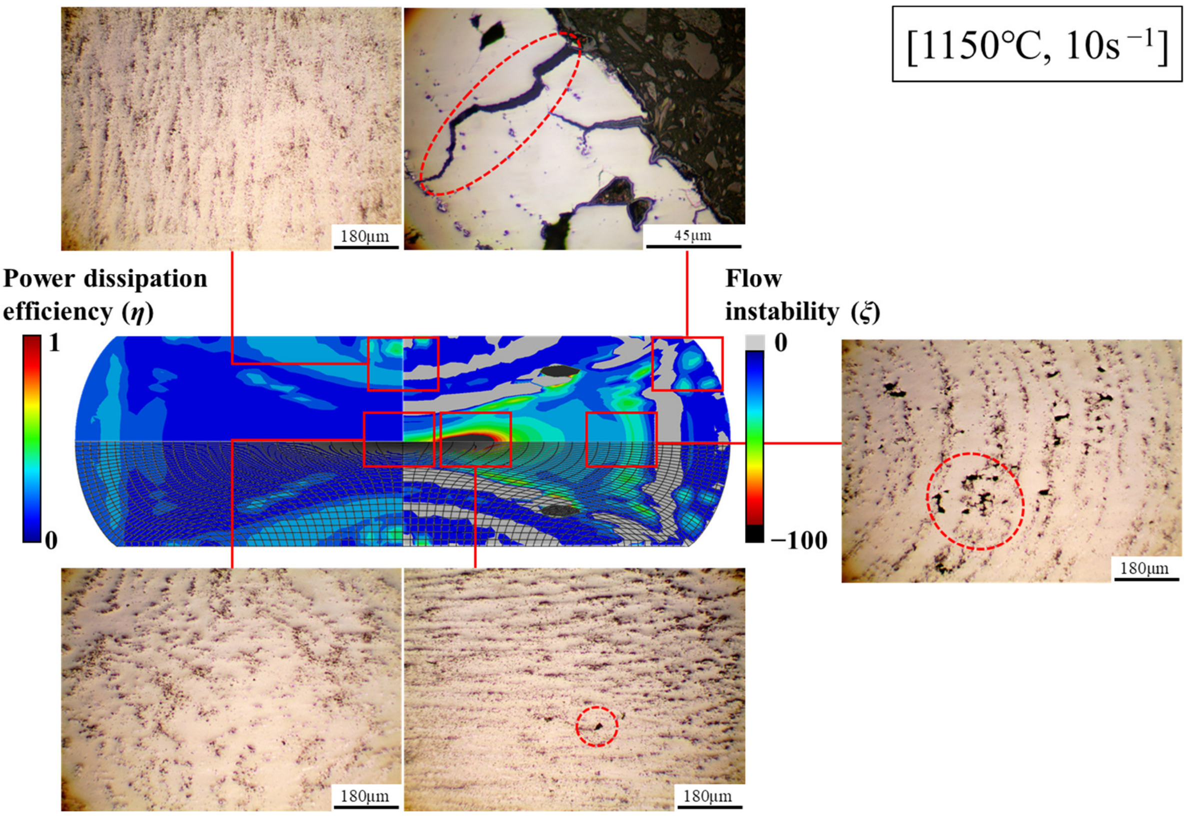

(**e**)

Figure 12. Distribution of η, ξ values at each deformation condition: (**a**) 900 °C/0.1 s^{-1}, (**b**) 1000 °C/0.1 s^{-1}, (**c**) 1100 °C/0.1 s^{-1}, (**d**) 1150 °C/0.01 s^{-1} and (**e**) 1150 °C/10 s^{-1}.

Figure 12a shows an unstable value ($\xi < 0$) at the periphery of region ⓑ, and the η value in the same area is relatively high compared to other regions. The interior of region ⓑ appears stable ($\xi > 0$), and the η value is low. Notably, wedge cracks are observed at the localized unstable region at the boundary between regions ⓐ and ⓑ. Figure 12b reveals unstable regions in all areas ⓐ, ⓑ and ⓒ, but region ⓐ has a higher η values area compared to the others. No significant microstructural defects are found in the remaining regions, except for the wedge crack observed at the boundary between regions ⓑ and ⓒ. The highest η value is shown at the boundary between regions ⓐ and ⓒ ($\xi < -100$). Figure 12c exhibits localized unstable values at the boundaries between regions ⓐ, ⓑ and regions ⓑ, ⓒ. It presents relatively high η values in areas without unstable regions. In the entire area, the highest η values are observed in region ⓒ and the center of the specimen. In region ⓑ with low unstable values, carbides are found to be clustered together. Figure 12d reveals coarse microstructural particles compared to other deformation conditions at 1100 °C or less. Unstable regions appear in all areas ⓐ, ⓑ and ⓒ, with intergranular cracks observed across the unstable areas. No microstructural defects are found in the stable region of ⓑ, and high η values are displayed in region ⓒ. Figure 12e also shows coarse microstructural particles, with intergranular cracks observed in most unstable regions. All regions generally exhibit a lower η value distribution than other deformation conditions. This trend is consistent with the 3D power dissipation efficiency map, indicating that the strain rate greatly influences η.

High temperatures can cause grain boundary weakening, making the material more susceptible to intergranular cracking. The strain rate at which the material is deformed can significantly influence the occurrence of intergranular cracking. High strain rates can lead to stress concentrations at the grain boundaries, promoting crack initiation and propagation along these boundaries. The stress state of the material can also affect the susceptibility to intergranular cracking. In areas where ξ is positive, no microstructural defects were found. Specifically, in the same deformation conditions, no microstructural defects were found in areas where the specimen's η was relatively high and ξ was positive. Considering both η and ξ will contribute to identifying and preventing the locations of microstructural defects. By analyzing these two parameters, it is possible to optimize the hot forging process, minimize defects and improve the overall material properties of the forged product.

5. Conclusions

The 3D flow instability map allows for the prediction of external crack occurrence. The 3D processing map and compressed specimen suggest that forging processes with a strain of 0.7 or higher at temperatures of 1100 °C or above result in defects in the forged product. The flow instability map and the surface of the compressed specimen enable the prediction of defects during forging.

Visual inspection of process conditions that avoid flow instability zones is facilitated by the 3D flow instability map stacked up to 1.0. To prevent instability during the hot forging processes, the strain rate should decrease as the strain increases, starting at a temperature of 1050 °C. Defect-free process conditions can be achieved within a narrow range of hot working conditions, specifically at temperatures between 1070 and 1140 °C and strain rates between 0.3 and 0.6 s^{-1}.

The integration of processing map theory and numerical simulation was accomplished using ABAQUS. The distribution tendency of η and ξ in ABAQUS corresponded well with the 3D processing map. Microstructural defects in forged products can be predicted using the method presented in this study. Moreover, the primary defect in the microstructure of M50 steel is the wedge crack, which is characterized as an intergranular crack.

In the numerical simulation based on the flow instability criterion proposed in this study, no microstructural defects were observed in the stable region where $\xi > 0$. Overall, cracks are found in the unstable region. The simulation results and microstructure analysis showed good agreement. Consequently, microstructural changes during hot working can be effectively predicted and utilized for decision making in the hot forging process.

Author Contributions: Conceptualization, J.P. and B.H.; methodology, J.P. and N.K.; software, B.H.; validation, J.P., B.H., H.K. and N.K.; formal analysis, J.P.; investigation, J.P.; resources, N.K.; data curation, B.H.; writing—original draft preparation, J.P.; writing—review and editing, N.K.; visualization, J.P. and B.H.; supervision, N.K.; project administration, H.K.; funding acquisition, H.K. All authors have read and agreed to the published version of the manuscript.

Funding: This work was supported by Korea Research Institute for Defense Technology Planning and Advancement-Grant funded by Defense Acquisition Program Administration (DAPA) (No. 20-107-E00-017-03).

Conflicts of Interest: The authors declare no conflict of interest.

References

1. Wei, Y.; Yu, X.; Su, Y.; Shen, X.; Xia, Y.; Yang, W. Effect of residual stress and microstructure evolution on size stability of M50 bearing steel. *J. Mater. Res. Technol.* **2021**, *10*, 651–661. [CrossRef]
2. Mukhopadhyay, P.; Kannaki, P.; Srinivas, M.; Roy, M. Microstructural developments during abrasion of M50 bearing steel. *Wear* **2014**, *315*, 31–37. [CrossRef]
3. Wang, F.; Qian, D.; Mao, H.; He, Y.; Shu, B. Evolution of microstructure and mechanical properties during tempering of M50 steel with Bainite/Martensite duplex structure. *J. Mater. Res. Technol.* **2020**, *9*, 6712–6722. [CrossRef]
4. Essa, F.; Elsheikh, A.H.; Yu, J.; Elkady, O.A.; Saleh, B. Studies on the effect of applied load, sliding speed and temperature on the wear behavior of M50 steel reinforced with Al2O3 and/or graphene nanoparticles. *J. Mater. Res. Technol.* **2021**, *12*, 283–303. [CrossRef]
5. Ali, M.K.A.; Xianjun, H. Improving the tribological behavior of internal combustion engines via the addition of nanoparticles to engine oils. *Nanotechnol. Rev.* **2015**, *4*, 347–358. [CrossRef]
6. Bridge, J.E.; Maniar, G.N.; Philip, T.V. Carbides in M-50 high speed steel. *Metall. Mater. Trans. B* **1971**, *2*, 2209–2214. [CrossRef]
7. Yu, X.; Zheng, D.; Yang, X.; Wang, S.; An, M.; Yan, G.; Xia, Y.; Xing, F. Effect of carbide precipitation behavior at high temperatures on microstructure and mechanical properties of M50 steel. *J. Mater. Res. Technol.* **2022**, *18*, 1155–1165. [CrossRef]
8. Jiang, H.; Song, Y.; Wu, Y.; Shan, D.; Zong, Y. Microstructure evolution and mechanical anisotropy of M50 steel ball bearing rings during multi-stage hot forging. *Chin. J. Aeronaut.* **2021**, *34*, 254–266. [CrossRef]
9. Semiatin, S.L.; Jonas, J.J. *Formability and Workability of Metals: Plastic Instability and Flow Localization*; American Society for Metals: Detroit, MI, USA, 1984; 299p.
10. Kumar, N.; Kumar, S.; Rajput, S.K.; Nath, S.K. Modelling of flow stress and prediction of workability by processing map for hot compression of 43CrNi steel. *ISIJ Int.* **2017**, *57*, 497–505. [CrossRef]
11. Sun, C.; Liu, G.; Zhang, Q.; Li, R.; Wang, L. Determination of hot deformation behavior and processing maps of IN 028 alloy using isothermal hot compression test. *Mater. Sci. Eng. A* **2014**, *595*, 92–98. [CrossRef]
12. Zhao, H.; Qi, J.; Su, R.; Zhang, H.; Chen, H.; Bai, L.; Wang, C. Hot deformation behaviour of 40CrNi steel and evaluation of different processing map construction methods. *J. Mater. Res. Technol.* **2020**, *9*, 2856–2869. [CrossRef]
13. Quan, G.-Z.; Liu, K.-W.; Jie, Z.; Bin, C. Dynamic softening behaviors of 7075 aluminum alloy. *Trans. Nonferrous Met. Soc. China* **2009**, *19*, s537–s541. [CrossRef]
14. Somani, M.; Birla, N.; Prasad, Y.; Singh, V. Microstructural validation of processing maps using the hot extrusion of P/M Nimonic AP-1 superalloy. *J. Mater. Process. Technol.* **1995**, *52*, 225–237. [CrossRef]
15. Frost, H.; Ashby, M. *Deformation-Mechanism Maps: The Plasticity and Creep of Metals and Ceramics*; Pergamon Press: Oxford, UK, 1982; 175p.
16. Ziegler, H. Some extremum principles in irreversible thermodynamics, with application to continuum mechanics. *Prog. Solid Mech.* **1963**, *4*, 93–193.
17. Kumar, A.K. Criteria for Predicting Metallurgical Instabilities in Processing. Master's Thesis, Indian Institute of Science, Bangalore, India, 1987.
18. Prasad, Y.; Gegel, H.; Doraivelu, S.; Malas, J.; Morgan, J.; Lark, K.; Barker, D. Modeling of dynamic material behavior in hot deformation: Forging of Ti-6242. *Metall. Trans. A* **1984**, *15*, 1883–1892. [CrossRef]
19. Gegel, H. Synthesis of atomistics and continuum modeling to describe microstructure. In *Computer Simulation in Materials Science: Papers Presented at the 1986 ASM Materials Science Seminar, Lake Buena Vista, FL, USA, 4–5 October 1986*; ASM: Detroit, MI, USA, 1986; pp. 291–344.
20. Murty, S.N.; Rao, B.N.; Kashyap, B. On the hot working characteristics of 2014 Al–20 vol% Al2O3 metal matrix composite. *J. Mater. Process. Technol.* **2005**, *166*, 279–285. [CrossRef]
21. Murty, N.S.; Rao, N.B.; Kashyap, B. Development and validation of a processing map for AFNOR 7020 aluminium alloy. *Mater. Sci. Technol.* **2004**, *20*, 772–782. [CrossRef]
22. Malas, J.C.; Seetharaman, V. Using material behavior models to develop process control strategies. *JOM* **1992**, *44*, 8–13. [CrossRef]

23. Semiatin, S.; Seetharaman, V.; Weiss, I. Hot workability of titanium and titanium aluminide alloys—An overview. *Mater. Sci. Eng. A* **1998**, *243*, 1–24. [CrossRef]
24. Samantaray, D.; Mandal, S.; Bhaduri, A. Characterization of deformation instability in modified 9Cr–1Mo steel during thermo-mechanical processing. *Mater. Des.* **2011**, *32*, 716–722. [CrossRef]
25. Murty, S.N.; Rao, B.N.; Kashyap, B. Identification of flow instabilities in the processing maps of AISI 304 stainless steel. *J. Mater. Process. Technol.* **2005**, *166*, 268–278. [CrossRef]
26. Jenab, A.; Taheri, A.K. Experimental investigation of the hot deformation behavior of AA7075: Development and comparison of flow localization parameter and dynamic material model processing maps. *Int. J. Mech. Sci.* **2014**, *78*, 97–105. [CrossRef]
27. El Hassani, F.B.; Chenaoui, A.; Dkiouak, R.; Elbakkali, L.; Al Omar, A. Characterization of deformation stability of medium carbon microalloyed steel during hot forging using phenomenological and continuum criteria. *J. Mater. Process. Technol.* **2008**, *199*, 140–149. [CrossRef]
28. Ma, X.; Zeng, W.; Wang, K.; Lai, Y.; Zhou, Y. The investigation on the unstable flow behavior of Ti17 alloy in α+ β phase field using processing map. *Mater. Sci. Eng. A* **2012**, *550*, 131–137. [CrossRef]
29. Liu, J.; Cui, Z.; Li, C. Analysis of metal workability by integration of FEM and 3-D processing maps. *J. Mater. Process. Technol.* **2008**, *205*, 497–505. [CrossRef]
30. Zhi, C.; Wu, Z.; Lei, J.; Huang, Z.; Xv, H.; Zhu, Y.; Jia, W.; Liu, P.; Ma, L. Deformation and Fracture Characterization of an Mg-Sn-Ca Alloy Using 3D Processing Maps. *Metals* **2023**, *13*, 645. [CrossRef]
31. Zhao, M.; Huang, L.; Li, C.; Li, J.; Li, P. Evaluation of the deformation behaviors and hot workability of a high-strength low-alloy steel. *Mater. Sci. Eng. A* **2021**, *810*, 141031. [CrossRef]
32. Park, J.; Kim, Y.; Shin, S.; Kim, N. Characterization of Hot Workability in AISI 4340 Based on a 3D Processing Map. *Metals* **2022**, *12*, 1946. [CrossRef]
33. Jeong, H.Y.; Park, J.; Kim, Y.; Shin, S.Y.; Kim, N. Processing parameters optimization in hot forging of AISI 4340 steel using instability map and reinforcement learning. *J. Mater. Res. Technol.* **2023**, *23*, 1995–2009. [CrossRef]
34. Ebrahimi, R.; Najafizadeh, A. A new method for evaluation of friction in bulk metal forming. *J. Mater. Process. Technol.* **2004**, *152*, 136–143. [CrossRef]
35. Kwak, T.; Lim, H.; Kim, W. Hot compression behavior of the ignition-resistant Mg–5Y–2.5 Zn–1.2 Ca alloy with long-period stacking ordered structures. *J. Alloys Compd.* **2015**, *632*, 417–428. [CrossRef]
36. Kwak, T.; Lim, H.; Kim, W. Hot compression characteristics and processing maps of a cast Mg–9.5 Zn–2.0 Y alloy with icosahedral quasicrystalline phase. *J. Alloys Compd.* **2015**, *644*, 645–653. [CrossRef]
37. Cai, D.; Xiong, L.; Liu, W.; Sun, G.; Yao, M. Characterization of hot deformation behavior of a Ni-base superalloy using processing map. *Mater. Des.* **2009**, *30*, 921–925. [CrossRef]
38. Xi, T.; Yang, C.; Shahzad, M.B.; Yang, K. Study of the processing map and hot deformation behavior of a Cu-bearing 317LN austenitic stainless steel. *Mater. Des.* **2015**, *87*, 303–312. [CrossRef]
39. Gao, Y.; Liu, X.; Chen, H.; Xue, X.; Gao, H.; Luo, W.; Wang, K.; Li, S.; Du, Y. Hot Workability and Microstructural Evolution of Ti-5.5 Al-5Mo-5V-2Nb-1Fe-1Zr Titanium Alloy Based on the Different Phase Zones during Plastic Deformation at High Temperatures. *Metals* **2023**, *13*, 92. [CrossRef]
40. Prasad, Y.; Rao, K.; Sasidhar, S. *Hot Working Guide: A Compendium of Processing Maps*; ASM International: Detroit, MI, USA, 2015.
41. Prasad, Y.; Seshacharyulu, T. Modelling of hot deformation for Microstructural control. *Int. Mater. Rev.* **1998**, *43*, 243–258. [CrossRef]
42. Li, B.; Pan, Q.; Yin, Z. Characterization of hot deformation behavior of as-homogenized Al–Cu–Li–Sc–Zr alloy using processing maps. *Mater. Sci. Eng. A* **2014**, *614*, 199–206. [CrossRef]
43. Prasad, M.; Inamdar, J. Effect of cement kiln dust pollution on black gram (*Vigna mungo* (L.) Hepper). *Proc. Plant Sci.* **1990**, *100*, 435–443. [CrossRef]
44. Ziegler, H. *An Introduction to Thermomechanics*; Elsevier: Amsterdam, The Netherlands, 2012.
45. Narayana Murty, S.; Nageswara Rao, B.; Kashyap, B. Instability criteria for hot deformation of materials. *Int. Mater. Rev.* **2000**, *45*, 15–26. [CrossRef]
46. KAMINENI, P.; Prasad, Y. Advanced techniques to evaluate hot workability of materials. In *Comprehensive Materials Processing: Advanced Forming Technologies*; Elsevier Ltd.: Amsterdam, The Netherlands, 2014; Volume 3, pp. 397–426.
47. Yang, Q.; Lei, L.; Fan, X.; Jia, Z.; Zhang, Z.; Li, W.; Liu, Q. Microstructure evolution and processing map of Al–Cu–Li–Mg–Ag alloy. *Mater. Chem. Phys.* **2020**, *254*, 123256. [CrossRef]
48. Wang, Y.; Zhao, G.; Xu, X.; Chen, X.; Zhang, C. Constitutive modeling, processing map establishment and microstructure analysis of spray deposited Al-Cu-Li alloy 2195. *J. Alloys Compd.* **2019**, *779*, 735–751. [CrossRef]
49. Seshacharyulu, T.; Medeiros, S.; Frazier, W.; Prasad, Y. Hot working of commercial Ti–6Al–4V with an equiaxed α–β microstructure: Materials modeling considerations. *Mater. Sci. Eng. A* **2000**, *284*, 184–194. [CrossRef]

50. Thamburaja, P.; Sarah, K.; Srinivasa, A.; Reddy, J. Fracture of viscoelastic materials: FEM implementation of a non-local & rate form-based finite-deformation constitutive theory. *Comput. Methods Appl. Mech. Eng.* **2019**, *354*, 871–903.
51. Sarah, K.; Thamburaja, P.; Srinivasa, A.; Reddy, J. Numerical simulations of damage and fracture in viscoelastic solids using a nonlocal fracture criterion. *Mech. Adv. Mater. Struct.* **2020**, *27*, 1085–1097. [CrossRef]